

Coherent Two Dimensional Infrared Spectroscopy of a Cyclic Decapeptide Antamanide. A Simulation Study of the Amide-I and A Bands

Cyril Falvo, Tomoyuki Hayashi, Wei Zhuang, and Shaul Mukamel*

Department of Chemistry, University of California—Irvine, Irvine, California

Received: February 19, 2008; Revised Manuscript Received: June 19, 2008

The two-dimensional infrared photon echo spectrum of Antamanide ($^{-1}\text{Val-}^2\text{Pro-}^3\text{Pro-}^4\text{Ala-}^5\text{Phe-}^6\text{Phe-}^7\text{Pro-}^8\text{Pro-}^9\text{Phe-}^{10}\text{Pro-}$) in chloroform is calculated using an explicit solvent molecular dynamics (MD) simulation combined with a density functional theory (DFT) map for the effective vibrational Hamiltonian. Evidence for a strong intramolecular hydrogen bonding network is found. Comparison with experimental absorption allows the identification of the dominant conformation. Multidimensional spectroscopy reveals intramolecular couplings and gives information on its dynamics. A two-color amide-I and amide-A crosspeak is predicted and analyzed in terms of local structure.

1. Introduction

Understanding the structure and folding dynamics of peptides in solution is an important challenge. 2D-NMR techniques introduced in the 1970s are an important structure determination tool with a microsecond time resolution.^{1,2} A large number of experimental and theoretical studies have been devoted to the development of femtosecond multidimensional techniques in the infrared, visible, and ultraviolet regions.^{3–11} In a 2D-IR photon echo experiment, three femtosecond pulses with wavevectors k_1 , k_2 , and k_3 interact with the molecule to generate a coherent signal which is heterodyne detected in the direction $k_l = -k_1 + k_2 + k_3$ (see Figure 1). The signal is recorded as a function of the three time delays between pulses.¹¹

2D-IR spectroscopy probes high frequency vibrations. The theoretical description of vibrations in peptides is much more complex than that of spin dynamics probed by NMR, and extracting structural information requires extensive modeling. IR techniques can determine the vibrational dynamics on much faster timescales than NMR. Numerous theoretical studies of 2D-IR have been conducted.^{12–21} A high level electronic structure simulation is necessary in order to accurately model the vibrational dynamics and spectra. Most theoretical approaches use a semiclassical treatment, where the high frequency optically active vibrations are treated quantum mechanically and all other degrees of freedom are treated as a classical bath giving rise to a fluctuating Hamiltonian. The determination of this Hamiltonian has been a topic of interest over the past few years.^{16–20} Several theoretical tools which combine electronic structure calculations, molecular dynamics and excitonic Hamiltonian description have been developed.^{18–20,22,23} Peptides have four amide vibrational modes (amide-I, II, III, and A) localized on the backbone peptide bonds and will be denoted local amide modes (LAMs). The vibrational Hamiltonian consists of the local amide Hamiltonian expanded in LAMs and their couplings between the different units. Most studies had focused on the amide-I band.^{19,22,23} Its frequency in solvent was calculated using a map, that connects it to the local electrostatic field. Such maps allow long time (nanosecond) molecular dynamics (MD) simulation.

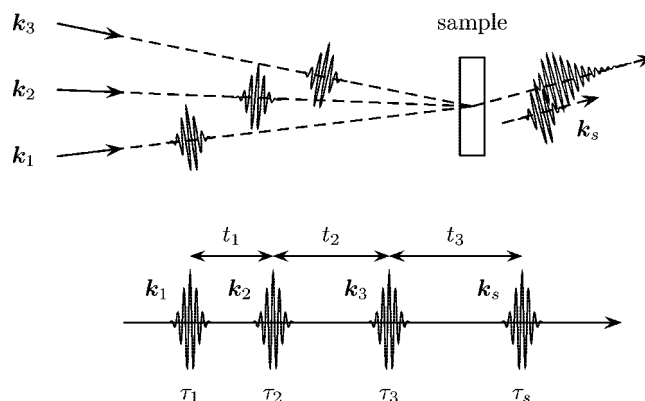


Figure 1. Coherent four wave mixing 2D-IR experiment.

We had developed an electrostatic density functional theory (DFT) map¹⁸ of all amide states in *N*-methylacetamide, a model of the peptide bond. The map provides a first-principles effective vibrational Hamiltonian which includes the fundamental, overtone, combination frequencies and transition moments of the amide-III, II, I, and A. It is based on vibrational eigenstate calculations of a sixth-order anharmonic DFT potential in the presence of up to a third-rank multipole (octapole) electric field. The map was first applied to the amide-I band combined with the ab initio map of Torii and Tasumi¹⁴ for the covalently bonded nearest neighbor couplings and transition dipole coupling model (TDC) for nonbonded units.^{12,13} We denote it as MAP1.¹⁹

An extension of this map, denoted here as MAP2, has been constructed in order to describe the amide-I band as well as other amide vibrational modes, including the vibration amide-A, amide-II, and amide-III¹⁸ using improved coupling models. For nearest covalently bonded units the ab initio map of Torii and Tasumi has been replaced by a higher level DFT map and for nonbonded units higher multipoles of the coupling have been included.²⁰

Highly accurate electrostatic maps are required in order to reproduce the variation of the vibration with its environment (molecule, solvent, and intramolecular hydrogen bond dynamics). The hydrogen bonding network is crucial for determining the structure and dynamics of peptide in solution. The sensitivity of vibrational spectra to hydrogen bonding has been studied in several systems^{24–27} including the decapeptide Antamanide.²⁶

* Corresponding author. E-mail: smukamel@uci.edu.

TABLE 1: Dihedral Angles (in degrees) of the Five Conformations Used As a Starting Point for the MD Simulations^a

	XRAY		A128		E116		G129		G193	
	Φ	Ψ								
¹ Val	-113	158	-96	105	-79	127	-97	146	-105	162
² Pro	-64	161	-70	133	-72	143	-76	133	-80	148
³ Pro	-80	-21	-93	17	-96	20	-106	43	-95	24
⁴ Ala	-103	-22	-98	83	-93	-45	-134	67	-93	-49
⁵ Phe	70	30	-87	40	67	35	-79	63	53	27
⁶ Phe	-78	161	-88	130	-89	126	-96	135	-140	135
⁷ Pro	-62	160	-68	144	-76	142	-80	140	-72	138
⁸ Pro	-92	-4	-92	22	-93	17	-95	18	-86	5
⁹ Phe	-101	-22	-96	-54	-95	-42	-112	54	-100	57
¹⁰ Phe	56	48	72	25	71	19	-58	71	-53	-4

^a XRAY denotes the structure of Antamanide in a crystal determined by X-ray crystallography.⁴⁰ A128, E116, G129, and G193 correspond to the four structures suggested by Blackledge et al.³⁹

TABLE 2: Average Dihedral Angles and Corresponding Standard Deviation (in degrees) of the XRAY and E116 Conformations^a

	XRAY				E116			
	$\langle\Phi\rangle$	σ_Φ	$\langle\Psi\rangle$	σ_Ψ	$\langle\Phi\rangle$	σ_Φ	$\langle\Psi\rangle$	σ_Ψ
¹ Val	-70.4	10.0	151.7	10.5	-71.5	10.0	154.9	8.0
² Pro	-68.1	6.9	157.1	8.0	-68.7	6.8	157.9	7.6
³ Pro	-80.3	7.7	11.3	8.3	-80.0	7.8	10.9	8.9
⁴ Ala	-80.9	9.0	-48.2	7.4	-81.2	9.1	-48.5	7.4
⁵ Phe	72.5	6.6	-51.1	8.6	72.5	6.7	-50.5	8.6
⁶ Phe	-72.0	10.2	156.3	8.3	-71.8	10.3	156.3	8.3
⁷ Pro	-67.5	6.7	157.6	7.5	-67.7	6.8	157.7	7.5
⁸ Pro	-79.3	7.4	8.1	8.4	-79.3	7.5	8.3	8.5
⁹ Phe	-80.3	9.0	-50.8	7.1	-80.7	9.0	-50.4	7.1
¹⁰ Phe	72.1	6.4	-48.5	9.0	72.3	6.4	-48.5	8.9

^a Calculations are made during the last 14 ns.

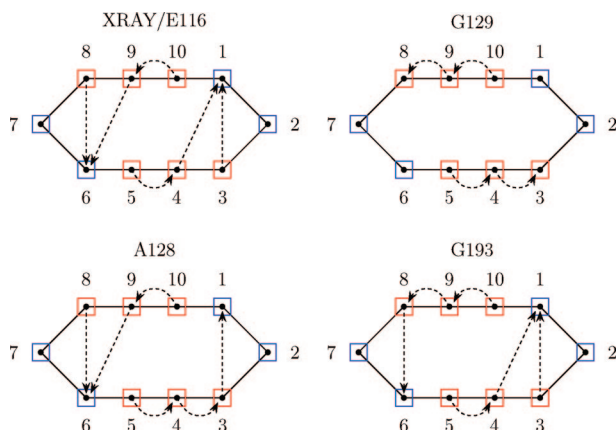


Figure 3. Hydrogen bonding network of the different average conformations. Each arrow links an N-H group to a C=O group. A hydrogen bond is defined if the distance $H \cdots O$ is smaller than 3.2 Å and the angle $N-H \cdots O$ is smaller than 60°.

For the XRAY/E116 conformation, we observe six hydrogen bonds, which is the maximum possible number. All six N-H vibrations are hydrogen bonded, two C=O groups are doubly bonded, two C=O vibrations are singly bonded, and the other four C=O are not bonded. This hydrogen bonding network has been pointed out previously by Moran et al.²⁶ They performed electronic structure calculation to determine the different possible structures, and the Kabsch-Sander criterion was used to determine the hydrogen bond network.⁴⁸

The average dihedral angles and associated standard deviations of A128 and G193 are given in Table 3. As in XRAY/E116, the angles Ψ_5 and Ψ_{10} show a significant deviation from their initial values. For both A128 and G193, Φ_6 also experi-

TABLE 3: Average Dihedral Angles and Corresponding Standard Deviation (in degrees) of the A128 and G193 Conformations^a

	A128				G193			
	$\langle\Phi\rangle$	σ_Φ	$\langle\Psi\rangle$	σ_Ψ	$\langle\Phi\rangle$	σ_Φ	$\langle\Psi\rangle$	σ_Ψ
¹ Val	-71.6	10.2	150.9	9.2	-121.7	24.1	154.6	7.3
² Pro	-68.5	7.0	152.9	7.6	-71.8	6.8	158.8	7.0
³ Pro	-80.6	7.9	5.1	8.9	-80.4	7.6	12.9	9.6
⁴ Ala	-90.0	9.1	70.1	8.5	-78.7	10.1	-57.5	7.9
⁵ Phe	-75.5	7.4	54.6	16.9	70.3	7.3	-45.6	11.6
⁶ Phe	-144.0	18.2	153.6	7.9	-71.2	10.7	143.3	11.4
⁷ Pro	-70.3	6.7	158.2	7.1	-67.1	7.1	152.2	7.9
⁸ Pro	-80.1	7.5	8.9	8.8	-80.2	7.7	4.8	8.4
⁹ Phe	-78.4	9.3	-58.1	7.5	-90.1	8.5	69.4	8.3
¹⁰ Phe	70.5	7.1	-45.6	10.9	-73.9	8.8	38.8	27.2

^a Calculations are made during the last 14 ns. In bold are highlighted the angles which experience larger deviations.

ences large relaxation. Starting from -88° and -140° , respectively, the angle relaxes to -144° and -71° for the conformations A128 and G193. For A128, we observe a non-negligible deviation for the angle Ψ_1 (from 105° to 151°). As a result, the average configurations A128 and G193 can be approximately deduced from each other by the symmetry $\Phi_n^{A128} \approx \Phi_{n+5}^{G193}$ and $\Psi_n^{A128} \approx \Psi_{n+5}^{G193}$. Both A128 and G193 experience relatively small fluctuations around their average structure (less than 12° for all angles except for two angles with large deviations $>15^\circ$ (in bold in Table 3)) indicating that these configurations are less stable. The trajectories of the angles with large deviations, Φ_6 and Ψ_5 for A128 and Φ_1 and Ψ_{10} for G193, are displayed in Figure 4.

Figure 3 also shows the hydrogen bond networks of A128 and G193. Unlike XRAY/E116, the hydrogen bond network of A128 and G193 does not have the symmetry of the molecule. However the network of one conformation can be deduced from the other by an n to $n + 5$ permutation of the amide groups. For G193, we recover the network observed by Moran et al.,²⁶ but this is not the case for A128. This previous study missed the symmetry A128/G193 observed here. In that study, the configurations were optimized using electronic structure calculations but the solvent was not explicitly included. As in XRAY/E116, all N-H modes are hydrogen bonded. However, for the C=O, we observe some differences. In both A128 and G193 configurations, one C=O is doubly bonded, four are singly bonded, and three are not bonded. These difference have clear signatures in the linear and nonlinear IR spectra.

The average and corresponding standard deviation of the dihedral angles of G129 are reported in the Table 4. As in XRAY/E116, G129 has approximately the $\Phi_n \approx \Phi_{n+5}$ and

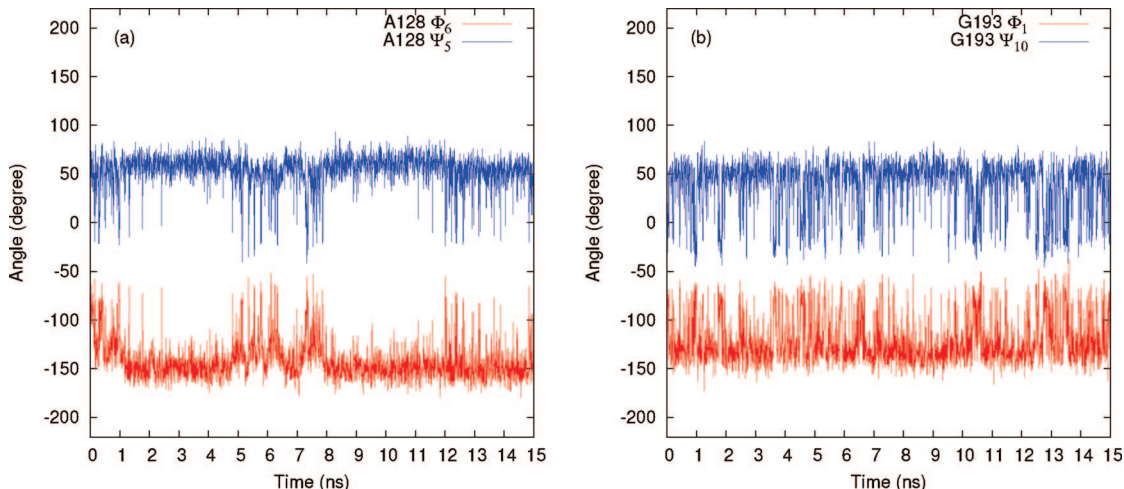


Figure 4. Time evolution of dihedral angles. (a) Evolution of Φ_6 and Ψ_5 for the A128 conformation. (b) Evolution of Φ_1 and Ψ_{10} .

$\Psi_n \approx \Psi_{n+5}$ symmetry. However this configuration experiences much larger deviations for several angles. As shown in Figure 5, the time evolution of the angles Ψ_1 , Ψ_4 , and Φ_4 shows that the fluctuations correspond to jumps between different states.

The hydrogen bond network of the average conformation G129 is sketched in Figure 3. Like the dihedral angles, the $n \rightarrow n + 5$ symmetry is observed. Unlike the other configurations where all N–H modes were hydrogen bonded, using our hydrogen bond criterion, we found that G129 has only four intramolecular hydrogen bonds and this configuration is thus less stable. The less restrictive criterion used in ref 39 yielded a fully hydrogen bonded structure. However, the two additional hydrogen bonds are weaker.

3. Effective Hamiltonian and Absorption Spectrum

We had used the simulation protocol of refs18 and 19 to generate a set of eigenenergies. As shown in Figure 2 because of the presence of four proline groups, four amide CO–NH out of ten units only contain isolated CO groups. Assuming that each unit contains one or two high frequency vibrations (amide-I only or both amide-I and amide-A), we write the following effective vibrational exciton Hamiltonian

$$H_S = \hbar \sum_{n=1}^{N_1} (\omega_{1n} B_{1n}^\dagger B_{1n} - A_{1n} B_{1n}^\dagger B_{1n}^2) + \hbar \sum_{n \neq m=1}^{N_1} J_{1nm} B_{1n}^\dagger B_{1m} + \hbar \sum_{n=1}^{N_2} (\omega_{2n} B_{2n}^\dagger B_{2n} - A_{2n} B_{2n}^\dagger B_{2n}^2) + \hbar \sum_{n \neq m}^{N_2} J_{2nm} B_{2n}^\dagger B_{2m} - \hbar \sum_{n=1}^{N_1} \sum_{m=1}^{N_2} K_{12nm} B_{1n}^\dagger B_{1n} B_{2m}^\dagger B_{2m} \quad (1)$$

where B_{1n}^\dagger , B_{1n} , B_{2n}^\dagger , and B_{2n} are boson creation and annihilation operators corresponding to amide-I and amide-A frequency vibration located on the n th local unit. ω_{1n} , A_{1n} , ω_{2n} , and A_{2n} are, respectively, the frequency and anharmonicity of the amide-I and amide-A vibration on the n th unit. We have $N_1 = 10$ amide-I local vibrations ($\omega_1 \approx 1650 \text{ cm}^{-1}$) and $N_2 = 6$ amide-A local vibrations ($\omega_2 \approx 3300 \text{ cm}^{-1}$). The two bands are well-separated. The intermode couplings are represented by the constants J_{1nm} and J_{2nm} which modify the eigenstates by inducing a delocalization of the vibrations. We have neglected the linear J coupling between the amide-I and the amide-A vibrations. Given the frequency mismatch $\omega_2 - \omega_1 \approx 1650 \text{ cm}^{-1}$, its effect on the eigenstates is small. On the other hand, we consider quartic

TABLE 4: Average Dihedral Angles and Corresponding Standard Deviation (in degrees) of the G129 Conformation^a

	G129			
	$\langle \Phi \rangle$	σ_Φ	$\langle \Psi \rangle$	σ_Ψ
¹ Val	-100.8	14.8	134.5	18.9
² Pro	-72.9	7.9	152.6	8.8
³ Pro	-80.8	7.9	1.6	9.4
⁴ Ala	-95.2	18.2	76.9	19.1
⁵ Phe	-77.4	8.5	76.3	18.6
⁶ Phe	-103.6	17.0	125.9	18.7
⁷ Pro	-71.1	8.3	152.0	9.9
⁸ Pro	-80.4	7.9	0.7	10.0
⁹ Phe	-90.8	10.4	75.2	12.1
¹⁰ Phe	-77.5	8.6	74.3	14.8

^a Calculations are made during the last 14 ns. In bold are highlighted the angles which experience larger deviations.

coupling between the amide-I and amide-A bands (K coupling) given by the constants K_{12nm} . This coupling is essentially local so that we simply set $K_{12nm} = \delta_{nm} K_{12nm}$. The dipole interaction with the optical field is given by

$$H_{\text{int}} = -E(t) \left[\sum_{n=1}^{N_1} \mu^{(1)} (B_{1n}^\dagger + B_{1n}) + \sum_{n=1}^{N_2} \mu^{(2)} (B_{2n}^\dagger + B_{2n}) \right] \quad (2)$$

where $\mu^{(1)}$ and $\mu^{(2)}$ are, respectively, the transition dipole of the amide-I and amide-A vibrations. The eigenvalues of the Hamiltonian H_S (eq 1) are sketched in Figure 6. Since we have neglected all interband relaxation processes and in particular the coupling between the amide-A and the amide-I band, we have three blocks: the ground state, the one, and the two exciton blocks.

Our MD simulations have generated an ensemble of configurations. For each configuration, we have calculated the Hamiltonian parameters and the corresponding eigenvalues and eigenvectors. The parameters were calculated using electronic structure calculations of MAP1¹⁹ and MAP2.^{18,20} MAP1 provides the parameters for the amide-I Hamiltonian only. The local amide-I frequencies (ω_{1n}) and its anharmonicities (A_{1n}) are parametrized with the multipole electric field on the local amide unit generated by the environment. The parametrization is based on the sixth-order anharmonic potential in five normal coordinates (including all four amide modes) of the model system (*N*-methylacetamide) constructed with DFT (BPW91/6-31G(d,p)) calculations. The linear amide-I couplings between the neighboring amide unit (J_{1nm}) are calculated by the Torii and Tasumi

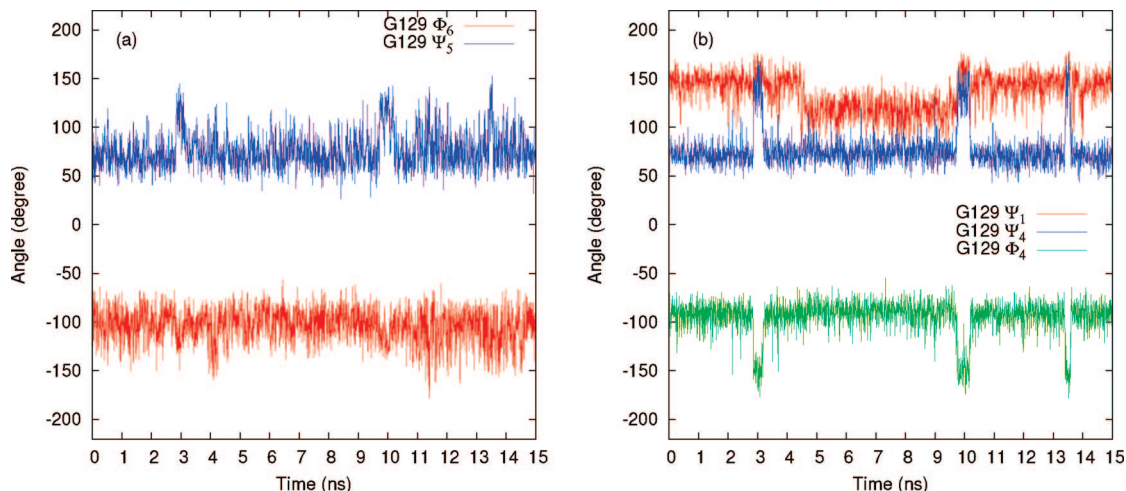


Figure 5. Time evolution of dihedral angles for G129 conformation. (a) Trajectory of Φ_6 and Ψ_5 . (b) Ψ_1 , Ψ_4 , and Φ_4 .

map,¹⁴ which is based on the Hartree–Fock ab initio calculations of the glycine dipeptide (GLDP) for different Ramachandran angles. Non-neighbor electrostatic couplings are given by the transition dipole coupling model.^{12,13} MAP2 provides the complete set of parameters for the peptide Hamiltonian of all four amide modes (I, II, III, and A) in the same way as MAP1 and also provides higher level neighbor and non-neighbor couplings. The linear neighboring couplings (J_{1nm} , J_{2nm}) and the nonlinear neighbor couplings (K_{12nm}) are parametrized by the Ramachandran angles based on the anharmonic vibrational potential of the GLDP constructed at the BPW91/6-31G(d,p) level. Non-neighbor electrostatic couplings are calculated by the transition multipole coupling mechanism including dipole–dipole ($\sim R^{-3}$), dipole–quadrupole ($\sim R^{-4}$), quadrupole–quadrupole, and dipole–octapole ($\sim R^{-6}$) interactions. These higher multipole interactions were found crucial for the amide-II, III, and A interactions.²⁰

Using our four MD trajectories (A128, E116, G129, and G193), we have performed the calculation of the vibrational absorption spectra of the amide-I and the amide-A region. The fluctuations of the eigenenergies and the eigenvectors at the femtosecond timescale are responsible for homogeneous and inhomogeneous broadening.^{11,49,50} In this study, slow inhomogeneous dephasing is included microscopically. Homogeneous dephasing (fast fluctuations) is added by a dephasing rate.^{11,49} $\Gamma = 5.5 \text{ cm}^{-1}$ for the amide-I band.^{5,19} $\Gamma = 22 \text{ cm}^{-1}$ for amide-A (assuming that the dephasing is scaled as the square of the energy $\Gamma \propto \epsilon^2$). We assume the same Γ for all transitions in each band. Our classical simulations generate an ensemble and the final signals are given by averaging over the various snapshots.

The linear absorption is given by

$$I(\omega) = \left\langle \sum_e \frac{\Gamma_e |\mu_{ge}|^2}{(\omega - \omega_e)^2 + \Gamma_e^2} \right\rangle \quad (3)$$

The average $\langle \cdot \cdot \cdot \rangle$ is over the distribution ω_e and μ_{ge} in the various snapshots, ω_e is the vibrational frequency of the excited state e , Γ_e is the homogeneous dephasing, and μ_{ge} is the transition dipole from the ground state to the excited state e .

The simulated linear absorptions using the two maps are displayed in Figure 7. For comparison, we show the experimental spectrum from ref 35. A 55 cm^{-1} redshift for MAP1 and a 58 cm^{-1} redshift for MAP2 was introduced to match theory and experiment.

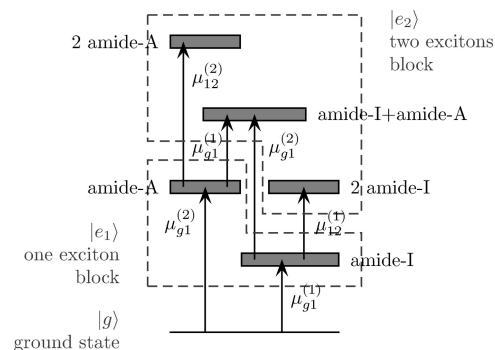


Figure 6. Energy scheme of the amide-A and amide-I bands.

Each configuration shows a specific absorption profile. MAP1 and MAP2 give similar lineshapes for all configurations except for G129. E116 shows two main peaks. For MAP2, the high frequency peak is located around 1670 cm^{-1} and the low frequency peak is located around 1629 cm^{-1} . The corresponding MAP1 frequencies are 1627 and 1671 cm^{-1} . Eigenvector analysis shows that the low frequency peak corresponds mainly to vibration located on the hydrogen bonded CO whereas the high frequency peak represents unbounded CO modes. G129 for MAP1 has one strong peak at 1646 cm^{-1} with a smaller one near 1670 cm^{-1} , whereas for MAP2, two peaks with equal intensity, located respectively at 1656 and 1669 cm^{-1} , are visible. A128 and G193 have three peaks. For MAP1 and MAP2, the low frequency peak of both configurations is located respectively near 1631 cm^{-1} . For A128, the central peak is located near 1649 cm^{-1} . For G193, this peak is only well-resolved for MAP1 at 1649 cm^{-1} , however for MAP2, a shoulder is visible near 1656 cm^{-1} . For G193, the last peak is located near 1666 cm^{-1} for both MAP1 and MAP2. For A128, the position of this peak depends on the map. It is located around 1663 cm^{-1} for MAP1 and near 1670 cm^{-1} for MAP2.

The sensitivity of the linear absorption in the map can be directly related to the localization length of the system. Using MAP2, we have calculated the amide-I average localization length defined as

$$L = \left\langle \frac{1}{N} \sum_{e=1}^{N_i} \frac{1}{\sum_m |\Psi_e(m)|^4} \right\rangle \quad (4)$$

where $\Psi_e(m)$ is the probability amplitude to find an amide-I exciton on the site m . For E116, we find $L = 2.0$, for G193,

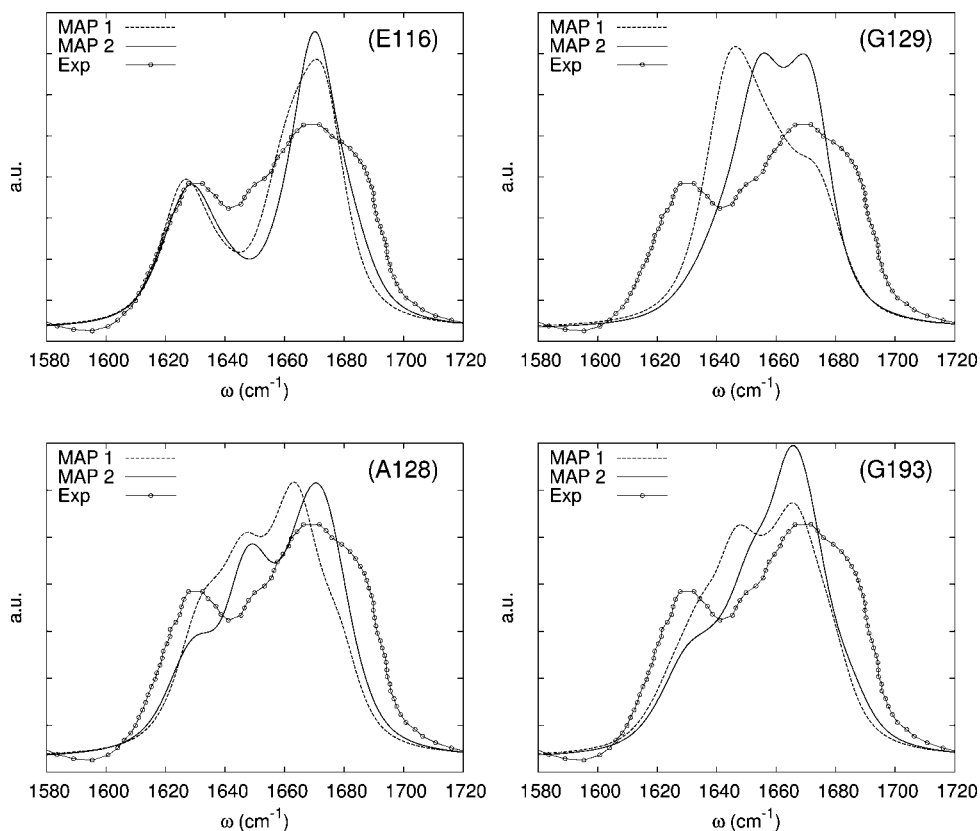


Figure 7. Linear absorption spectra of the four conformations: solid line (MAP2), dashed line (MAP1), open circle (experiment).³⁵ To match with experiment, a 55 cm^{-1} red-shift for MAP1 and a 58 cm^{-1} red-shift for MAP2 are introduced.

$L = 2.1$, for A128, $L = 2.4$, and for G129, $L = 2.8$. Consequently, the amide-I exciton is much more delocalized in G129 than in the other conformations and the corresponding eigenstates are more sensitive in the couplings between the vibrational groups which is the major difference between MAP1 and MAP2. In the same spirit, E116 is the less delocalized configuration and also the less sensitive to the coupling.

The absorption of Antamanide in chloroform has been measured in the amide-I and amide-A region by Ivanov et al.^{34,35} The amide-I shows one main peak at 1668 cm^{-1} and a small peak at 1630 cm^{-1} . The experimental spectrum is very similar to our simulated E116, suggesting that this configuration is dominant. As was pointed out previously,³⁶ the conformation of this molecule strongly depends on the solvent and in particular in its ability to form hydrogen bonds with the molecule. Since MAP2 is based on a higher level of theory than MAP1, in the remainder of this study, we will focus on MAP2.

The linear absorption spectra of the amide-A band for all configurations are shown in Figure 8a. A 150 cm^{-1} red-shift was introduced to match with experiment. For all configurations, the amide-A band is much broader than the amide-I ($\sim 140\text{ cm}^{-1}$ compared to $\sim 70\text{ cm}^{-1}$). A128 and G193 have a similar shape characterized by an asymmetric peak near 3340 cm^{-1} with longer tail to the red. G129 is broader with a maximum at 3330 cm^{-1} , but the asymmetric shape is similar. E116 is narrower than G129 but has a more symmetric band with a main peak at 3330 cm^{-1} and a shoulder at 3300 cm^{-1} . The overall spectrum is red-shifted compared to the other configurations. Due to both their strong asymmetric shape and relatively small width, the configurations A128 and G193 fail to reproduce the experimental spectrum (see Figure 8a). G129 has the broadest absorption, close to the experimental ($\sim 130\text{ cm}^{-1}$ compared to 140 cm^{-1}); E116 is narrower ($\sim 105\text{ cm}^{-1}$) but has a more

symmetric shape, in better agreement with the experimental absorption. From the amide-A absorption, both G129 and E116 seem to play a role in the dynamics.

No jump between the different configurations was observed during our MD simulations; however, such transitions could occur on a much longer timescale which has been suggested by NMR. In that case, two or more conformers could give a contribution to the spectrum. We have investigated the linear absorption using a distribution of different conformers. However none of them improve drastically the shape of the spectrum. In Figure 8b is displayed the linear absorption in the amide-I band using a mixture of E116 and G129 conformers with a proportion ranging from 0% to 50% of G129. All spectra have been normalized to the low frequency peak. Increasing the G129 proportion causes the high frequency peak to become broader. Indeed we increase the inhomogeneous fluctuations. Since G129 does not have significant optical density in the 1625 cm^{-1} frequency range, the ratio between the intensity of the low frequency peak and the intensity of the high frequency peak decreases. However even for pure E116, this ratio is smaller than the experimental one (respectively ~ 0.5 and ~ 0.7). The differences between experimental spectrum and simulations are more likely to come from the limitations of our theoretical model than from a superposition of different conformer absorptions.

4. One-Color 2D-IR Photon Echo: Simulation of the Amide-I and A Bands

We now turn to the simulation of the 2D-IR photon echo signal in the amide-I and amide-A regions. Three quantum pathways contribute to the signal, as shown by the Feynmann diagrams (Figure 9): the ground-state bleaching (GSB), the excited-state emission (ESE), and the excited-state absorption

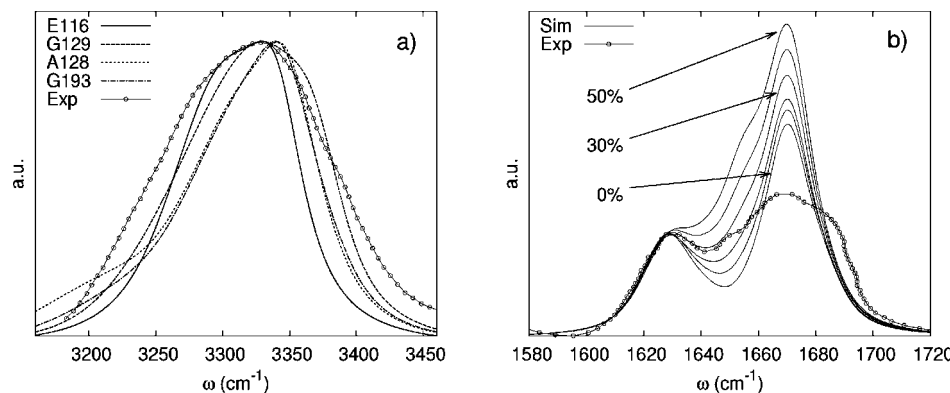


Figure 8. (a) Linear absorption spectrum of all possible configurations in the amide-A region: open circle, experimental data. A red-shift of 150 cm^{-1} has been introduced to correct our theoretical data. (b) Linear absorption spectra of a mixture E116/G129 ranging from 0% of G129 to 50% of G129: open circle, experimental data.

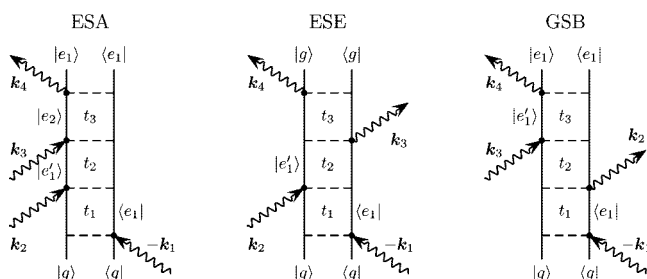


Figure 9. Feynman diagrams characterizing the three elementary processes of the photon echo: the excited-state absorption (ESA), the excited-state emission (ESE), and the ground-state bleaching (GSB).

(ESA). The GSB and the ESE both give a negative contribution to the spectrum and probe the one-exciton block. The ESA contribution is positive and probes the two-exciton block. The signal, recorded as a function of the three time intervals between the pulses (t_1 , t_2 , and t_3), is given by the response function of the third order $S(t_1, t_2, t_3)$ (see ref 49). A double Fourier transform is applied over the times t_1 and t_3 (see ref 10) and the signal is finally displayed as

$$S(\Omega_1, t_2, \Omega_3) = \int_0^{\infty} dt_1 \int_0^{\infty} dt_3 S(t_1, t_2, t_3) e^{i\Omega_1 t_1 + i\Omega_2 t_2} \quad (5)$$

The third-order response function $S(t_1, t_2, t_3)$ was calculated using the sum-over-states (SOS) expressions eq 5.19 of ref 11 as implemented in the Spectron code.¹⁹

We assume pulses short enough to cover the entire amide-I or the amide-A bandwidth. The splitting of the two bands ($\sim 1650 \text{ cm}^{-1}$) is large, and interband coherence cannot be created by a single color pulse. We used a rectangular pulse shape centered around 1650 cm^{-1} with a spectral width of 250 cm^{-1} for the amide-I region and centered around 3315 cm^{-1} with a spectral width of 500 cm^{-1} for the amide-A region. All transitions inside one band are excited equally and interband transitions are not possible.

2D-IR photon echo spectra of the amide-I region for all four configurations are displayed in Figure 10, both the imaginary part and the absolute value of the signal are shown. In the imaginary part, pairs of negative and positive peaks are observed in all cases. GSB and ESE give negative contributions along the diagonal corresponding to transitions between the ground state and the first excited states. The ESA gives rise to positive peaks associated with the negative peaks but red-shifted along Ω_3 . This red-shift comes directly from the anharmonicities $2A_{1n}$ of each vibrational mode. Measurement of the interval between

the negative and positive peaks gives a typical value of 15 cm^{-1} , in good agreement with measurement of the amide-I anharmonicity.^{51,52}

For E116, we identify the two main peaks observed previously in the absorption spectrum. Due to the elimination of inhomogeneous broadening by the photon echo,⁴⁹ these two peaks are well-resolved. Neither the imaginary part nor the absolute value signals show crosspeaks; however, we can identify some off-diagonal tails which come from the weak coupling between the two types of vibrational modes. Both high frequency and low frequency peaks have a similar diagonal and off-diagonal width. For the absorption of G129, two overlapping peaks were observed. In the 2D-IR photon, these two peaks are well-resolved with crosspeaks. Note that one crosspeak overlaps with the ESA contribution of the high frequency peak, reducing its intensity. For A128, we clearly observe three peaks with strong crosspeaks. These crosspeaks indicate coupling between the different modes and imply delocalization of exciton. For G193, only two peaks are well resolved; however, a diagonal red tail is observed in the absolute value of the signal near the high frequency peak. By comparing the tails of the different peaks in all configurations, we notice that E116 and G193 has the smallest tails whereas G129 and A128 have the strongest. As described previously, A128 and G129 have a greater delocalization length than the other two configurations, indicating a stronger influence of the couplings between the local modes.

The 2D-IR photon echo spectra in the amide-A region are shown in Figure 11. As noted for the linear absorption, all spectra are much broader than the amide-I region. By using larger homogeneous dephasing, we have increased the bandwidth; however, by looking at the diagonal bandwidth, we also see that inhomogeneous dephasing is very large in the amide-A region. The negative to positive peak splitting gives a value of 35 cm^{-1} for the anharmonicity of the NH vibration. This is smaller than previous measurement and calculation of the NH anharmonicity ($\sim 60 \text{ cm}^{-1}$),⁵² reflecting the accuracy of our map. As for the central frequency of both amide-I and amide-A bands, the anharmonicity requires an overall red-shift. However, we believe that the fluctuations around this value are well-represented by our simulation. In the amide-A region, differences between spectra of the various configurations are not as clear as in the amide-I region due to the large homogeneous and inhomogeneous bandwidth. Unlike 1D-IR, in a 2D-IR spectrum, homogeneous and inhomogeneous dephasing are separated. The diagonal width of the spectrum indicates inhomogeneous dephasing and the off-diagonal width characterizes the homogeneous dephasing. All spectra show a similar off-

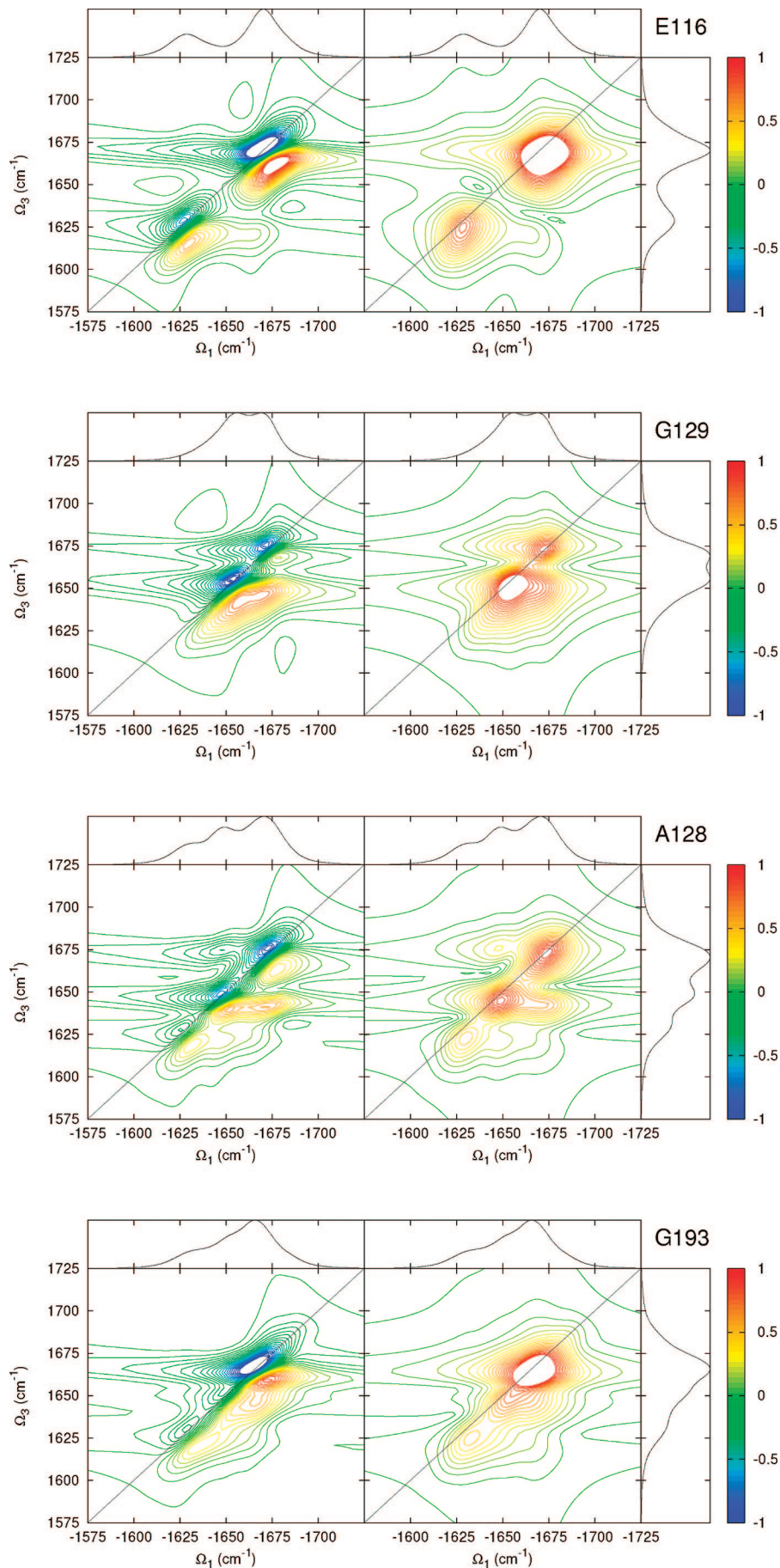
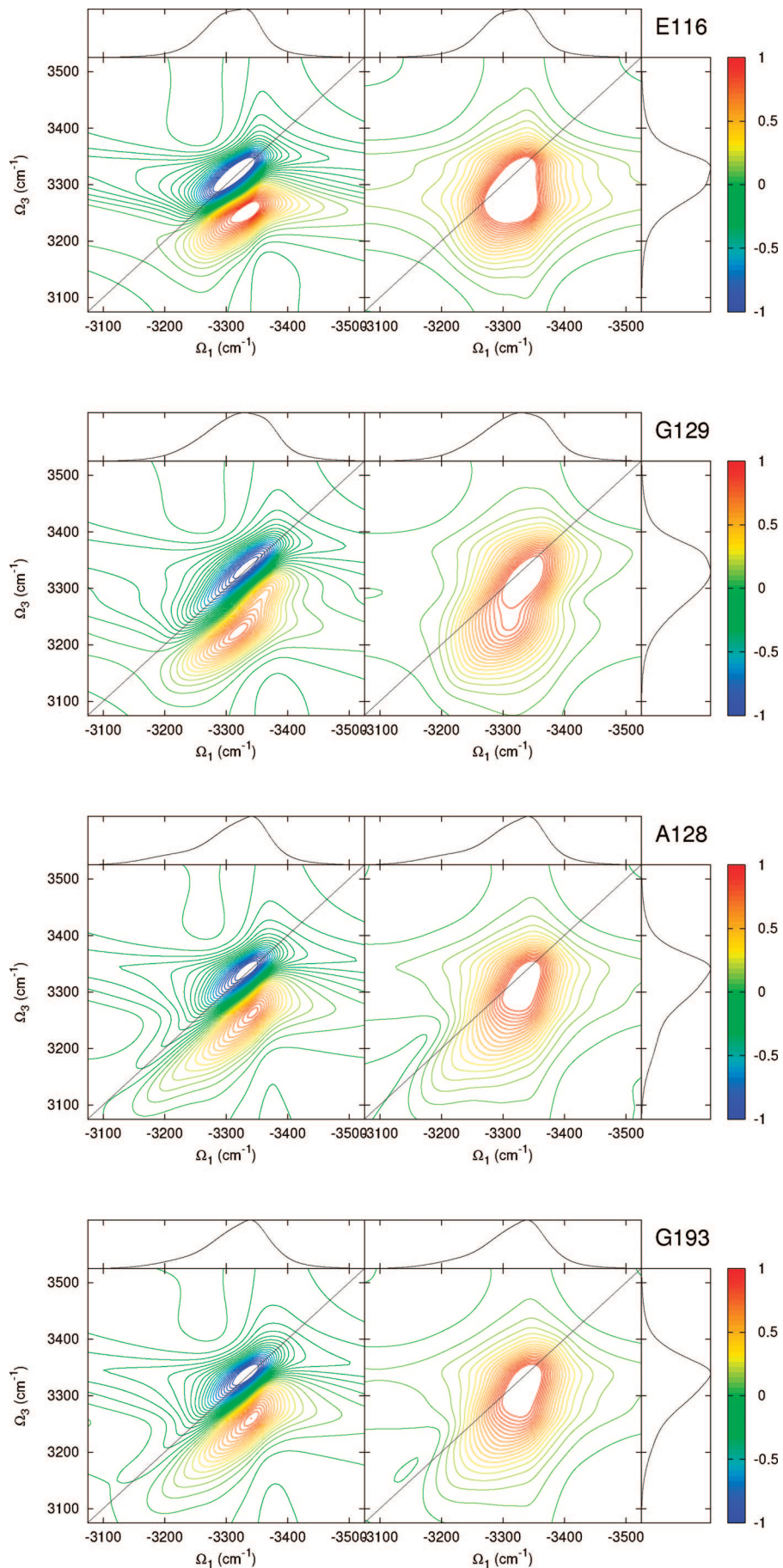


Figure 10. 2D-IR photon echo amide-I spectra for all conformations. (left) Imaginary part of the signal. (right) Absolute value of the signal.

**Figure 11.** 2D-IR photon echo amide-A spectra for all conformations. (left) Imaginary part of the signal. (right) Absolute value of the signal.

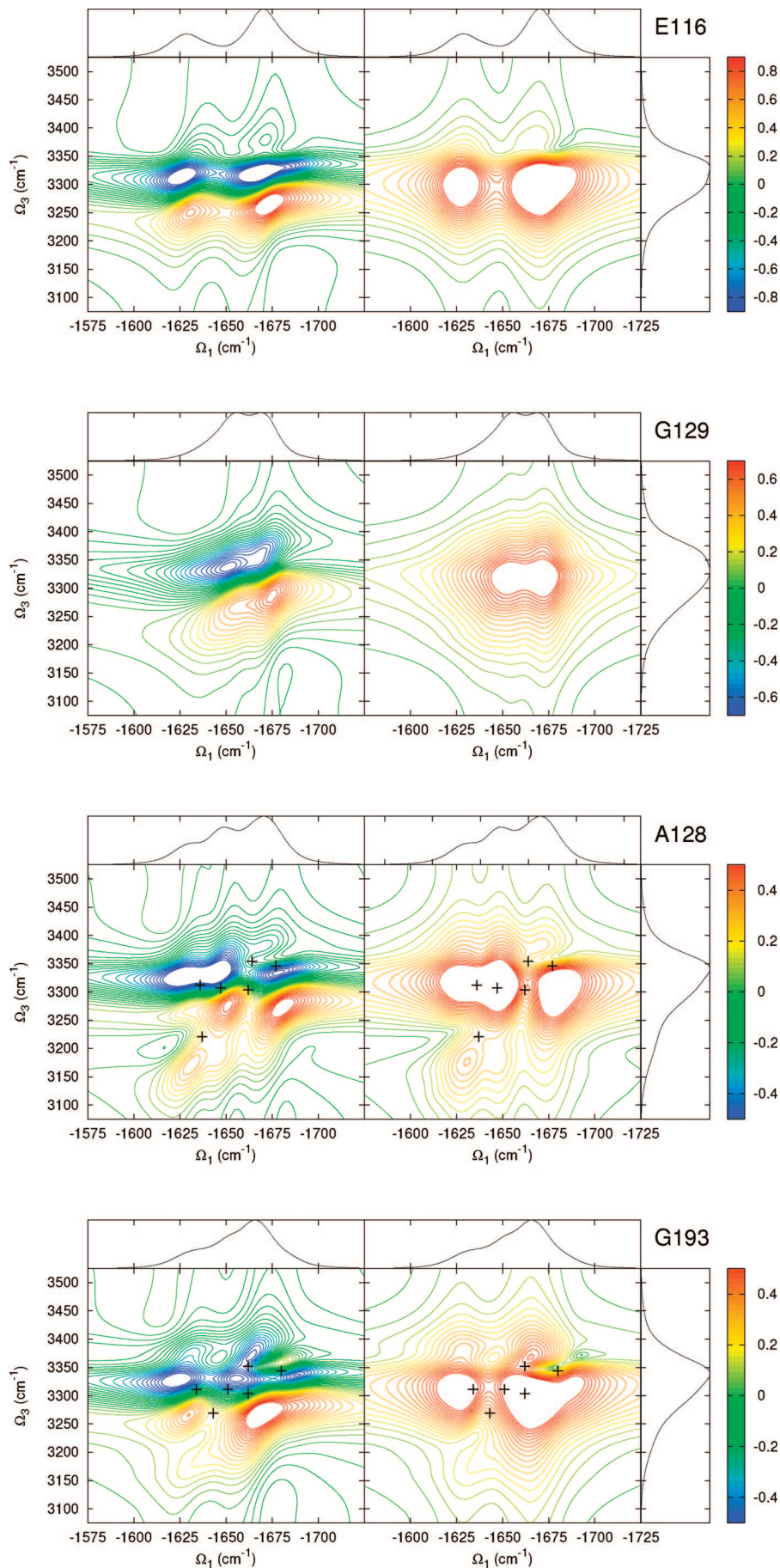


Figure 12. 2D-IR photon echo two-color spectra of all conformations. (left) Imaginary part of the signal. (right) Absolute value of the signal. For A128 and G193, the six averaged local frequencies of amide groups 3, 4, 5, 8, 9, and 10 (see Figure 3) are marked by a cross.

diagonal width. Indeed, we used a single dephasing parameter to describe the fast dynamics in all conformations. However, the diagonal width depends on the conformer. As noticed in the linear absorption, G129 has the broadest line shape among all configurations. Due to a lower number of intramolecular hydrogen bonds, the configuration G129 is less stable. This large inhomogeneous dephasing can be attributed to larger fluctuations of the molecular structure.

5. Two-Color 2D-IR Photon Echo: Simulation of the Amide-I/Amide-A Crosspeak

In a two-color experiment, the first two pulses span the $\omega_1 \sim 1650 \text{ cm}^{-1}$ amide-I band, and the other two are tuned to the $\omega_2 \sim 3315 \text{ cm}^{-1}$ amide-A band. This technique measures the amide-I/amide-A crosspeak. With this pulse configuration, only two Feynman diagrams, ESA and GSB, contribute to the signal. Indeed, for the third diagram, ESE occurs during the interaction with the third laser (frequency ω_2); however, the system has only been previously excited by the first two lasers to states with energy around ω_1 . ESA probes the amide-I + amide-A states. These states represent one exciton amide-I and one exciton amide-A interacting through the quartic coupling K_{12mn} .

The two-color spectra (imaginary part and absolute value) of all conformations are displayed in Figure 12. All spectra show an ensemble of pairs of negative and positive peaks. For two isolated vibrational modes with frequencies ω_1 and ω_2 coupled by a nonlinear coupling K_{12} without fluctuations, the two-color spectrum is given by a negative peak at (ω_1, ω_2) and a positive peak at $(\omega_1, \omega_2 - K_{12})$. The intensity of the peaks is directly proportional to the nonlinear coupling. For E116, the spectrum shows two pairs of peaks along the amide-I band corresponding to the two absorption modes observed previously. Surprisingly, both pairs have a similar intensity, which was not the case for the one-color experiment and the linear absorption. Since the coupling K_{12mn} between the amide-I and the amide-A band is local, only six amide groups are sensitive to this spectroscopic technique, the amide group numbers 3, 4, 5, 8, 9, and 10 (see Figure 3). The high frequency band is mainly given by the amide groups 3, 5, 9, and 10 (unbonded CO groups), and the low frequency band is mainly given by the amide groups 4 and 8 (hydrogen bonded CO groups). Because both pairs of peaks have a similar intensity, the K coupling of the low frequency modes should be approximately twice as strong as the K coupling of the high frequency mode. Indeed, by analyzing our Hamiltonian parameters, we found that $K_{12mn} \sim 13 \text{ cm}^{-1}$ for the low frequency modes while $K_{12mn} \sim 6 \text{ cm}^{-1}$ for the high frequency modes. G129 has one pair of equal intensity peaks. Since those two peaks are strongly overlapping, no local information on the system can be extracted from this spectrum. In A128 and G193 situations, in contrast, the spectra contains some features which can be interpreted in terms of local structure. Indeed, since 4 of the 10 amide groups do not interact with the amide-A band, a part of the inhomogeneous fluctuations has been removed. Moreover, some amide-I modes are coupled to different frequency interval of the amide-A band. The optical response is given in terms of the eigenstates of the system and not in terms of local structure. However, in peptides the eigenvalues are overlapping and it is in general difficult to keep track of the eigenstates. Consequently, we tried to interpret the 2D-IR two-color spectra of A128 and G193 in terms of local frequencies. Of course, the coupling between the modes changes the position of the absorption band and modifies quantitatively our interpretation; however qualitatively, we can detect some local information in those spectra. For A128 and G193, we have

computed the six averaged local frequencies (both amide-I and amide-A) corresponding to the modes 3, 4, 5, 8, 9, and 10. Those frequencies has been reported in the spectra (Figure 12). The average frequencies cannot account for the strong fluctuations occurring in the system and thus do not account in general for the spectra. However, we can see that for A128 the peak located around $(-1630, 3180) \text{ cm}^{-1}$ is most likely due to the amide group 5 (see Figure 3) with the average local frequency located at $(-1637, 3321) \text{ cm}^{-1}$. The tail located near $(-1660, 3375) \text{ cm}^{-1}$ due to the local mode 3 whose average frequency is $(-1664, 3354) \text{ cm}^{-1}$. For G193, the same tail is observed and can be assigned to the local mode 8 with the average frequency $(-1662, 3352) \text{ cm}^{-1}$.

6. Conclusions

We have used a combined MD, electronic structure protocol to study the nonlinear infrared response of Antamanide. MD simulations were performed in chloroform starting from four conformations suggested by NMR spectroscopy and the X-ray structure. These five trajectories yield only four different structures. We have compared two DFT maps for the effective vibrational Hamiltonian of the amide-I and amide-A bands. By comparing the absorption spectra using MAP1 and MAP2 with experiment, we found one conformation (E116) with a strong intramolecular hydrogen bond network to be dominant. MAP2 based on a higher level of theory was then used to simulate the linear absorption of the amide-A and showed a good agreement with experiment. We then used MAP2 to predict the 2D-IR photon echo spectra of the amide-I and amide-A bands. We showed that the small couplings between vibrational groups induce crosspeaks in the spectra. We have observed that when the excitons are more delocalized, the crosspeaks were more intense. We also noticed that conformation G129 which experiences larger fluctuations yields a broader spectrum. Finally, we proposed a two-color experiment in order to probe the amide-I/amide-A crosspeak. This spectrum reflects the nonlinear K coupling between the amide-I and the amide-A band. Since only some of the amide modes are sensitive to this coupling, some inhomogeneous fluctuations are removed. For two configurations, some spectral feature has been also interpreted in terms of local structure.

Extracting local information from IR spectroscopy (linear and nonlinear) is always a difficult task. 2D-IR, in general, does not probe structure but the vibrational dynamics governed by local anharmonicity and couplings between modes (J and K). Moreover, the interplay of different phenomena increases also the difficulty of the interpretation. However, in some situations, in particular in medium-sized molecules like Antamanide, IR spectroscopy, being sensitive to the intramolecular hydrogen bonding network, can be used as a complementary tool to NMR spectroscopy. Moreover, 2D spectroscopic techniques such as photon echo, double quantum coherence, chirality²¹ has the power to extract the specificity of each molecule. For a molecule with a strong intramolecular hydrogen bonding network similar to Antamanide, a two-color experiment, revealing the amide-I/amide-A crosspeak, can be an efficient technique. However, for larger molecules, this technique will not be effective since by increasing the inhomogeneous fluctuations we increase the overlapping between ESA and GSB contributions resulting in a vanishing spectrum.

Acknowledgment. The authors wish to thank Dr. Darius Abramavicius for many helpful discussions. The support of the National Institutes of Health (Grant No. GM-59230) and the

National Science Foundation (Grant No. CHE-0745892) is gratefully acknowledged.

References and Notes

- (1) Ernst, R. R.; Bodenhausen, G.; Wokaun, A. *Principles of nuclear magnetic resonance in one and two dimensions*; Oxford University Press: New York, 1995.
- (2) Wuthrich, K. *NMR of Proteins and Nucleic Acids*; Wiley-Interscience: New York, 1986.
- (3) Zanni, M. T.; Hochstrasser, R. M. *Curr. Opin. Struct. Biol.* **2001**, *11*, 516.
- (4) Ge, N.-H.; Hochstrasser, R. M. *Phys. Chem. Commun.* **2002**, *5*, 17.
- (5) Fang, C.; Wang, J.; Kim, Y. S.; Charnley, A. K.; Barber-Armstrong, W.; A. B.; Smith, I.; Decatur, S. M.; Hochstrasser, R. M. *J. Phys. Chem. B* **2004**, *108*, 10415.
- (6) Brixner, T.; Stenger, J.; Vaswani, H. M.; Cho, M.; Blankenship, R. E.; Fleming, G. R. *Nature* **2005**, *434*, 625.
- (7) Zigmantas, D.; Read, E. L.; Mancal, T.; Brixner, T.; Gardiner, A. T.; Cogdell, R. J.; Fleming, G. R. *Proc. Natl. Acad. Sci. USA* **2006**, *103*, 12672.
- (8) Parkinson, D. Y.; Lee, H.; Fleming, G. R. *J. Phys. Chem. B* **2007**, *111*, 7449.
- (9) Chergui, M., private communication.
- (10) Mukamel, S. *Annu. Rev. Phys. Chem.* **2000**, *51*, 691.
- (11) Mukamel, S.; Abramavicius, D. *Chem. Rev.* **2004**, *104*, 2073.
- (12) Krimm, S.; Bandekar, J. *J. Adv. Protein Chem.* **1986**, *38*, 181.
- (13) Torii, H.; Tasumi, M. *J. Chem. Phys.* **1992**, *96*, 3379.
- (14) Torii, H.; Tasumi, M. *J. Raman Spectrosc.* **1998**, *29*, 81.
- (15) Decius, W. E. B.; Cross, J. C. *Molecular Vibrations: The Theory of Infrared and Raman Vibrational Spectra*; McGraw-Hill: New York, 1955.
- (16) Cheatum, C. M.; Tokmakoff, A.; Knoester, J. *J. Chem. Phys.* **2004**, *120*, 8201.
- (17) Cha, S.; Ham, S.; Cho, M. *J. Chem. Phys.* **2002**, *117*, 740.
- (18) Hayashi, T.; Zhuang, W.; Mukamel, S. *J. Phys. Chem. A* **2005**, *109*, 9747.
- (19) Zhuang, W.; Abramavicius, D.; Hayashi, T.; Mukamel, S. *J. Phys. Chem. B* **2006**, *110*, 3362.
- (20) Hayashi, T.; Mukamel, S. *J. Phys. Chem.* **2007**, *11*, 11032.
- (21) Zhuang, W.; Hayashi, T.; Mukamel, S. *Angew. Chem.*, in press.
- (22) Ham, S.; Cho, M. *J. Chem. Phys.* **2003**, *118*, 6915.
- (23) la Cour Jansen, T.; Knoester, J. *J. Chem. Phys.* **2006**, *124*, 044502.
- (24) Fecko, C. J.; Eaves, J. D.; Loparo, J. J.; Tokmakoff, A.; Geissler, P. L. *Science* **2003**, *301*, 1698.
- (25) Torii, H.; Tatsumi, T.; Kanazawa, T.; Tasumi, M. *J. Phys. Chem. B* **1998**, *102* (1), 309.
- (26) Moran, A. M.; Park, S.-M.; Mukamel, S. *J. Chem. Phys.* **2003**, *118*, 9971.
- (27) la Cour Jansen, T.; Hayashi, T.; Zhuang, W.; Mukamel, S. *J. Chem. Phys.* **2005**, *123*, 114504.
- (28) Brüschweiler, R.; Roux, B.; Blackledge, M.; Griesinger, C.; Karplus, M.; Ernst, R. R. *Biochemistry* **1993**, *32*, 10960.
- (29) Schmidt, J. M.; Brüschweiler, R.; Ernst, R. R.; R. L.; Dunbrack, J.; Joseph, D.; Karplus, M. *J. Am. Chem. Soc.* **1993**, *115*, 8747.
- (30) Brunne, R. M.; van Gunsteren, W. F.; Brüschweiler, R.; Ernst, R. R. *J. Am. Chem. Soc.* **1993**, *115*, 8747.
- (31) Bremi, T.; Brüschweiler, R.; Ernst, R. R. *J. Am. Chem. Soc.* **1997**, *119*, 4272.
- (32) Wieland, T. *Angew. Chem., Int. Ed.* **1968**, *7*, 204.
- (33) Wieland, T.; Faulstich, H. *Crit. Rev. Biochem.* **1978**, *5*, 185.
- (34) Ivanov, V. T.; Miroshnikov, A. I.; Abdullaev, N. D.; Senyavina, L. B.; Arkhipova, S. F.; Uvarova, N. N.; Khalilulina, K. K.; Bystrov, V. F.; Ovchinnikov, Y. A. *Biochem. Biophys. Res. Commun.* **1971**, *42*, 654.
- (35) Ivanov, V. T.; Miroshnikov, A. I.; Koz'min, S. A.; Meshcheryakova, E. N.; Senyavina, L. B.; Uvarova, N. N.; Khalilulina, K. K.; Zabrodin, V. A.; Bystrov, V. F.; Ovchinnikov, Y. A. *Chem. Nat. Compd.* **1975**, *9*, 353.
- (36) Patel, D. J. *Biochemistry* **1973**, *12*, 667.
- (37) Kessler, H.; Bats, J. W.; Lautz, J.; Müller, A. *Liebigs Ann. Chem.* **1989**, 913.
- (38) Brüschweiler, R.; Blackledge, M. J.; Ernst, R. R. *J. Biomol. NMR* **1991**, *1*, 3.
- (39) Blackledge, M. J.; Brüschweiler, R.; Griesinger, C.; Schmidt, J. M.; Xu, P.; Ernst, R. R. *Biochemistry* **1993**, *32*, 10960.
- (40) Karle, I. L.; Wieland, T.; Schermer, D.; Ottenheim, H. C. J. *Proc. Natl. Acad. Sci. USA* **1979**, *76*, 1532.
- (41) Kalé, L.; Skeel, R.; Bhandarkar, M.; Brunner, R.; Gursoy, A.; Krawetz, N.; Phillips, J.; Shinozaki, A.; Varadarajan, K.; Schulten, K. *J. Comp. Phys.* **1999**, *151*, 283.
- (42) MacKerell, A. D., Jr.; Bashford, D.; Bellott, M.; Dunbrack, R. L., Jr.; Evanseck, J. D.; Field, M. J.; Fischer, S.; Gao, J.; Guo, H.; Ha, S.; Joseph-McCarthy, D.; Kuchnir, L.; Kuczera, K.; Lau, F. T. K.; Mattos, C.; Michnick, S.; Ngo, T.; Nguyen, D. T.; Prodhom, B.; Reiher, W., III; Roux, B.; Schlenkrich, M.; Smith, J. C.; Stote, R.; Straub, J.; Watanabe, M.; Wiórkiewicz-Kuczera, J.; Yin, D.; Karplus, M. *J. Phys. Chem. B* **1998**, *102*, 3586.
- (43) Fox, T.; Kollman, P. A. *J. Phys. Chem. B* **1998**, *102*, 8070.
- (44) Darden, T.; York, D.; Pedersen, L. *J. Chem. Phys.* **1993**, *98*, 10089.
- (45) Essmann, U.; Perera, L.; Berkowitz, M. L.; Darden, T.; Pedersen, L. G. *J. Chem. Phys.* **1995**, *103*, 8577.
- (46) Tu, K.; Tobias, D. J.; Klein, M. L. *Biophys. J.* **1995**, *69*, 2558.
- (47) Feller, S. E.; Zhang, Y.; Pastor, R. W.; Brooks, B. R. *J. Chem. Phys.* **1995**, *103*, 4613.
- (48) Kabsch, W.; Sander, C. *Biopolymers* **1983**, *22*, 2577.
- (49) Mukamel, S. *Principles of Nonlinear Optical Spectroscopy*; Oxford University Press: New York, 1995.
- (50) Tanimura, Y. *J. Phys. Soc. Jpn.* **2006**, *75*, 082001.
- (51) Hamm, P.; Lim, M.; Hochstrasser, R. M. *J. Phys. Chem. B* **1998**, *102*, 6123.
- (52) Wang, J.; Hochstrasser, R. M. *J. Phys. Chem. B* **2006**, *110*, 3798.